Journal of Southeast University (English Edition) Vol. 36, No. 2, pp. 163 - 169 June 2020 ISSN 1003—7985

Analysis and design of excitation system in homopolar inductor machine

Fu Xinghe Fu Xiangda Xu Yutian He Hang

(School of Electrical Engineering, Southeast University, Nanjing 210096, China)

Abstract: The excitation system of the homopolar inductor machine (HIM) is analyzed and designed to establish the design approach and evaluation criteria of the excitation system. The finite element method is used to calculate the three-dimensional electromagnetic field in the HIM, and the distribution and characteristics of the magnetic field are described. The analytical method is applied to investigate the design process of the excitation winding. The ratio of the axial length of the armature winding to the excitation winding and the ratio of the axial length of the working air-gap to the non-working air-gap are investigated by the numerical calculation method. A prototype HIM is designed and manufactured, and some experiments are implemented to verify the correctness of the theoretical analysis and numerical calculation results. The research results show that the established design method of the excitation winding is practical and feasible. Under the conditions of constant excitation magnetomotive force or constant excitation power, the optimum range of the axial length ratio of the armature winding and the excitation winding is 0.45 to 0.5. The optimal axial length of the non-working air-gap can be determined by the ratio of the stator inner diameter and pole-pairs.

Key words: homopolar inductor machine; excitation system; exciting coil; axial length ratio

DOI: 10.3969/j.issn.1003-7985.2020.02.006

The homopolar inductor machine (HIM) has the favorable advantages of an adjustable air-gap magnetic field, robust rotor structure, high reliability, and low idling losses. As a result, the HIM has renewed interest as an appealing candidate in flywheel energy storage[1] and capacitor charge power supply[2]. The power or torque density of the HIM is not high enough due to the homopolar magnetic field. Therefore, a multi-unit out-rotor HIM is proposed to boost the output power and stored energy[3]. Another investigated four-stator-cores HIM, which consists of an alternator and a motor, enjoys the merits of a high-voltage and high-frequency discharge performance[4]. A novel excitation compensation method is proposed to improve the power density as a capacitor charge power supply by installing a compensation winding[5]. Furthermore, the novel HIM with multistage stator cores is developed to solve the low power density owing to the length limitation and homopolar air-gap flux density[6].

The homopolar air-gap flux density in the HIM raises another question whether the analytical methods applied to the conventional machine can be used on the HIM? The controversy whether the two-reaction theory is applicable or not to the HIM is settled and it is applicable to the HIM[7]. Moreover, it is feasible to regard the HIM as a wound field synchronous machine (WFSM) or a combination of a WFSM and synchronous reluctance machine, which helps to simplify the HIM analysis[8]. An essential 3D flux distribution in the HIM brings more challenges to predicting machine behavior[9] since 3D finite element analysis (FEA) is a quite tough and time-consuming task when optimization design is implemented[10-11]. A nonlinear equivalent magnetic circuit and an air-gap permeance function are introduced to avoid the 3D magnetic field calculation[12]. Furthermore, a 2D analytical model is proposed to calculate the magnetic field and back-EMF (electromotive force)[13].

The relationship between the flux density in the working air-gap with the arced slot and the salient in the HIM is analyzed by using the finite element method (FEM)[14]. The optimal geometrical parameters of the tooth are obtained to achieve the maximum back-EMF in the armature winding[15]. The non-overlapping coils are used to obtain the maximal fundamental winding factor and back-EMF in a 32 kW HIM[16]. The core loss in the HIM with DC-biased magnetic induction is different from that in the conventional electrical machine with sinusoidal induction[17]. The inductance mathematic model and characteristics are presented and analyzed[18], and the operation mode of the HIM is discussed[19]. The performances of the HIM with a diode-bridge rectifier and capacitive load are analyzed, and the simplified average value mathematical model is established[20]. Narayanan et al.[21] developed an interesting HIM with three sections of the rotor, in which two sections work as alternators, and another section works as a motor.

Some investigations described the characteristics of the HIM in detail. However, except for the peripheral space

Received 2019-12-29, **Revised** 2020-04-20.

Biography: Fu Xinghe (1978—), male, doctor, associate professor, fuxinghe@seu.edu.cn.

Foundation item: The National Natural Science Foundation of China (No. 51977035).

Citation: Fu Xinghe, Fu Xiangda, Xu Yutian, et al. Analysis and design of excitation system in homopolar inductor machine[J]. Journal of Southeast University (English Edition), 2020, 36(2): 163 - 169. DOI: 10.3969/j.issn.1003-7985.2020.02.006.

competitions between the stator teeth and armature conductors, the axial space competitions between the armature windings and the excitation coils must be considered when designing the HIM. How to resolve this conflict and how to properly allocate the limited axial length are vital to the performance improvement of the HIM. At present, they are far from being adequately addressed.

This paper investigates the excitation system of the HIM by analytical and numerical methods. The magnetic field distribution of the HIM is revealed by finite element calculation. The design principle of the excitation coil in the HIM is discussed in detail, and an example is presented to illustrate the design process. The axial length ratios are investigated. The optimal parameters under different constraint conditions are predicted. Finally, a prototype HIM is manufactured, and some experiments are implemented to verify the correctness of the finite element calculation and theoretical analysis.

1 Structure and Magnetic Field

The schematic structure of the HIM is shown in Fig. 1. The HIM comprises of a 9-slots stator core with three-phase concentrated windings, a rotor with 4-teeth and 4-slots, excitation coils, and a frame. The excitation coils are fixed by the coil brackets and placed between the end windings and the end cap. Since there is no brush for the excitation coils, less maintenance is required for the HIM. In Fig. 1, the lines with arrows denote the flux path. The flux generated by the excitation current goes axially through the rotor yoke, then radially through the working air-gap into the stator teeth, then axially along the frame, again radially inward passing the non-working air-gap, and finally returns to the rotor yoke. The magnetic field of the HIM is a complex 3D field. Therefore, 3D finite element computation is required to illustrate the machine performance. Fig. 2 shows the flux distribution in the HIM under no-load, which is consistent with the theory analysis above.

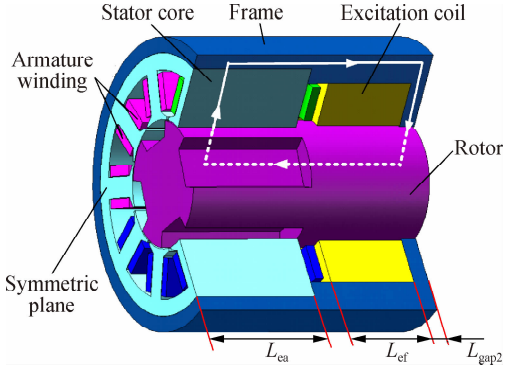

Fig. 1 Section view of the HIM

Fig. 2 shows that both the working and non-working air-gap magnetic fields are homopolar fields. For the non-working air-gap, the magnetic field is almost constant.

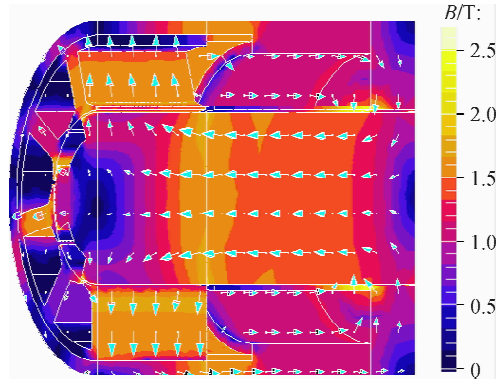

Fig. 2 Three-dimensional magnetic field of the HIM

But to the working air-gap, the magnetic field looks like a rectangle waveform with low values under the rotor slots and high values under the rotor teeth. Besides, the magnetic field in the working air-gap changes along the axial direction, which is quite different from the traditional electrical machine, such as the induction motor, PMSM, and WFSM. The homopolar and uneven magnetic field makes it challenging to design the HIM. The calculated line-to-line back-EMF in the HIM under no-load and rated speed is shown in Fig. 3. The waveforms are close to sinusoidal ones, although there are specific harmonic components.

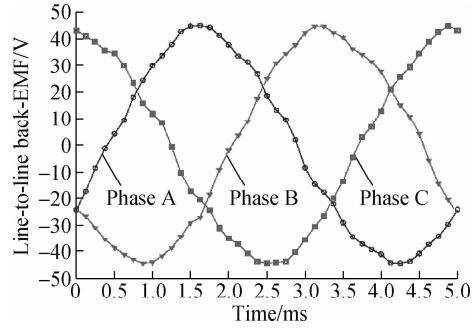

Fig. 3 Waveforms of the back-EMF in the HIM

2 Excitation Coil Design

The magnetomotive force F generated by the excitation current is defined as

$$F = NI_{\mathrm{f}} \tag{1}$$

where N is the number of turns of the excitation coil, and the exciting current I_{f} is expressed as

$$I_{\mathrm{f}} = \frac{U_{\mathrm{f}}}{R_{\mathrm{f}}} \tag{2}$$

where U_{f} is the voltage of the field power supply; R_{f} is the resistance of the exciting coil and R_{f} is given as

$$R_{\mathrm{f}} = \rho k_{\mathrm{t}} \frac{l_{\mathrm{sum}}}{s_{\mathrm{cu}}} = \frac{\rho k_{\mathrm{t}} N l_{\mathrm{ave}}}{\pi d_{\mathrm{cu}}^2 / 4} \tag{3}$$

where ρ is the resistivity of the copper; k_{t} is the temperature coefficient of the resistivity, and $k_{\mathrm{t}} = 1$ at normal

temperature; l_{sum} is the total length of the excitation coil; S_{cu} is the cross-section area of the excitation wire; d_{cu} is the diameter of the excitation wire; l_{ave} is the average length per turns of the excitation coil and l_{ave} is given as

$$l_{ave} = \pi D_{ave} = \frac{\pi}{2}(D_{out} + D_{in}) \tag{4}$$

where D_{ave} is the average diameter of the virtual cylinder annulus filled by the excitation coil; D_{out} is the outer diameter of the cylinder annulus; and D_{in} is the inner diameter of the cylinder annulus.

According to Eqs. (1) to (4), the magnetomotive force F can be rewritten as

$$F = NI_f = \frac{U_f d_{cu}^2}{2\rho k_t (D_{out} + D_{in})} \tag{5}$$

Eq. (5) shows that diameter d_{cu} of the excitation wire is determined when the excitation magnetic potential, excitation voltage, and outer and inner diameters of the cylinder filled by the excitation coil are constant. The excitation magnetic potential has nothing to do with the number of turns of the field winding.

The exciting power P_f can be expressed as

$$P_f = \frac{U_f^2}{R_f} = \frac{U_f^2 d_{cu}^2}{2\rho k_t N (D_{out} + D_{in})} \tag{6}$$

Eq. (6) shows that the excitation power is inversely proportional to the number of turns of the field winding.

The axial cross-section area S of the virtual cylinder annulus can be defined as

$$S = \frac{Nd^2}{k_{slot}} = \frac{2F\rho k_t (D_{out} + D_{in}) d_{cu}^2}{U_f k_{slot} d_{cu}^2} N = k_s N = \frac{1}{2} L_{ef} (D_{out} - D_{in}) \tag{7}$$

where k_{slot} is the copper space factor of the excitation coil; J is the electric current density; L_{ef} is the axial length of the virtual cylinder annulus; k_s is a comprehensive coefficient and it is given as

$$k_s = \frac{2F\rho k_t (D_{out} + D_{in}) d_{cu}^2}{U_f k_{slot} d_{cu}^2}$$

The above analysis shows that the relationships between the magnetomotive force, the exciting power, the exciting current, and the number of turns of the field winding are relatively complicated. Fig. 4 describes the complicated relationships when the magnetomotive force F and the exciting voltage U_f are constant.

Suppose that the axial cross-section area S locates at point A. According to Eq. (7), an appropriate point C on the vertical coordinates can be determined. Then, according to Eqs. (5) and (6), points D, E, and F can be calculated, respectively.

An example is given to verify the effectiveness of the proposed method. Given that $F = 1\ 000$ A, $U_f = 31$ V, $\rho = 1.678 \times 10^{-8}\ \Omega \cdot$ m, $k_t = 1$, $D_{out} = 68$ mm, $D_{in} = 47$ mm, $L_{ef} = 46$ mm, and $k_{slot} = 0.8$, we can obtain the calculation results as follows: $S = 4.83 \times 10^{-4}$ m^2, $N = 2\ 395$, $I_f = 0.42$ A, $P_f = 13$ W, $d_{cu} = 0.35$ mm, and $J = 4.3$ A/mm^2.

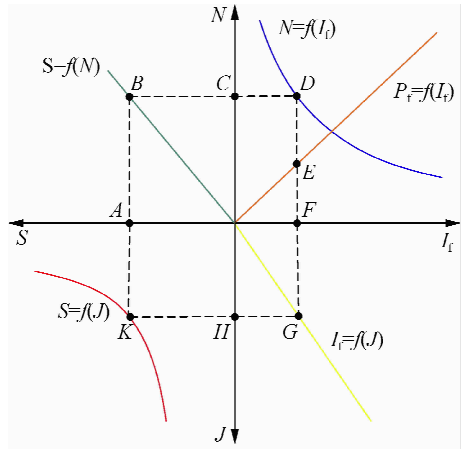

Fig. 4 Relationships between the variables in the process of the excitation coil design

3 Numerical Analysis of Axial Length Ratio

3.1 Axial length ratio of the armature winding to the excitation coil

Ignoring the axial length of the end winding and the end cap, the whole axial length L_e of the HIM mainly depends on the axial length L_{ef} of the virtual cylinder annulus filled by the excitation coil and the axial length L_{ea} of the armature winding, which means that

$$L_e = L_{ea} + L_{ef} \tag{8}$$

The ratio of the two axial lengths may affect the operating characteristic of the HIM when L_e is constant. Therefore, coefficient γ_L is defined as

$$\gamma_L = \frac{L_{ea}}{L_{ea} + L_{ef}} \tag{9}$$

The influences of the magnetomotive force and the exciting power on the electromagnetic design are considered. Therefore, the following two cases are discussed based on the finite element method.

Suppose that the total magnetomotive force generated by the excitation current is constant. The calculated flux linkage coefficient φ of the armature winding and the calculated exciting power P_f with different γ_L are shown in Fig. 5. Here, coefficient φ is defined as the ratio of the flux linkage to the number of turns of the armature winding. Fig. 5 shows that coefficient γ_L may affect the values of the output voltage and the exciting power. It is helpful to increase the axial length of the armature winding to produce a greater back-EMF. However, a longer axial length of the armature winding can lead to more excitation power. Moreover, when coefficient γ_L exceeds a critical value, the change rate of the flux linkage coefficient de-

creases, and the change rate of the exciting power increases. For the curves in Fig. 5, the utilization rate of the exciting power reaches a maximum when the two curves have the longest vertical distance. For the physical parameters of the test HIM, the proper coefficient γ_L should be in the range of 0.45 to 0.47. Therefore, according to the defined parameters ($L_{ef}=46$ mm) above, L_{ea} should be close to 40 mm.

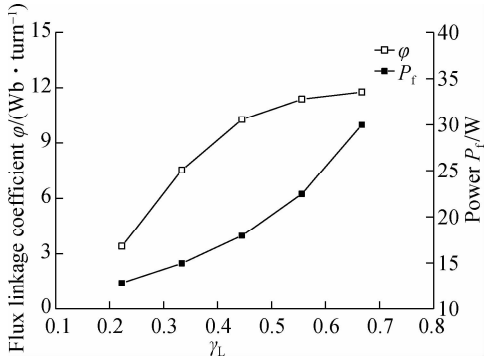

Fig. 5 Flux linkage and exciting power with constant magnetomotive force

Suppose that the exciting power is constant. With the increase in coefficient γ_L, the calculated flux linkage coefficient φ of the armature winding, and the calculated magnetomotive force F are presented in Fig. 6. When coefficient γ_L is small, the magnetic saturation appears in the stator core of the HIM owing to a shorter axial length of the armature winding and larger field ampere-turn. As a result, the flux linkage and the back-EMF with a smaller γ_L are lower than those with a larger γ_L. With the increase in γ_L, the flux linkage increases. When coefficient γ_L exceeds a critical value, both the flux linkage and the back-EMF decrease owing to a smaller axial length of L_{ef} and less magnetomotive force. Therefore, the proper coefficient γ_L is in the range of 0.45 to 0.5, which is almost consistent with the above results.

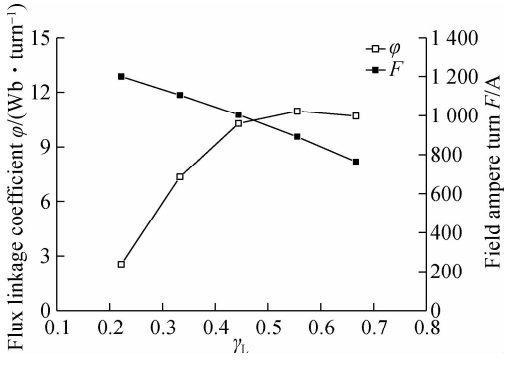

Fig. 6 Flux linkage and field ampere-turn with constant exciting power

3.2 Axial length ratio of the working air-gap to the non-working air-gap

There are two air-gaps in the HIM: the working air-gap and the non-working air-gap. The radial lengths of the two air-gaps are the same. However, the axial length of the non-working air-gap is less than that of the working air-gap, and the circumferential length of the non-working air-gap is greater than that of the working air-gap. Therefore, the magnetic reluctances of the two air-gaps are different. The effective air-gap flux density in the HIM may be affected by the magnetic reluctance of the two air-gaps. Under the action of 1 000 A field ampere-turn, the flux density in the two air-gaps with specific parameters ($L_{ea}=40$ mm, $L_{gap2}=8$ mm) are calculated by the finite element method as shown in Fig. 7. The flux density in the non-working air-gap reaches 1.7 T, while in the working air-gap, it is only 0.6 T. Therefore, the axial length ratio of the two air-gaps is quite vital and should be investigated to improve the density of the working air-gap.

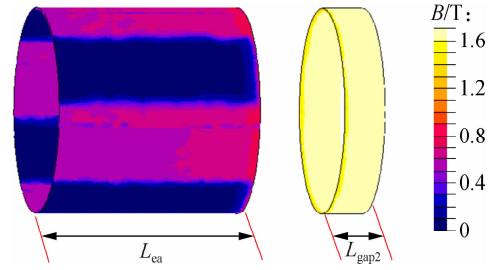

Fig. 7 Flux density in the working air-gap and the non-working air-gap

A coefficient k_{sg} is defined as

$$k_{sg}=\frac{S_{shaft}}{S_{gap2}}=\frac{\pi(D-2l_\delta)^2/4}{\pi(D-2l_\delta)L_{gap2}}=\frac{D-2l_\delta}{4L_{gap2}} \tag{10}$$

where S_{shaft} is the cross-section area of the shaft; S_{gap2} is the circumferential area of the non-working air-gap; D is the inner diameter of the stator iron; L_δ is the radial length of the two air-gaps.

Eq. (10) can be substituted by Eq. (11) since L_δ is much smaller than D.

$$k_{sg}=\frac{D}{4L_{gap2}} \tag{11}$$

To avoid saturation, suppose that coefficient k_{sg} is equal to 1. Therefore, L_{gap2} should be equal to $D/4$.

To consider the magnetic saturation in the HIM, a magnetic calculation based on the FEM is implemented to validate the analysis process above. The inner diameter D of the stator iron is 45 mm. Also, the total axial length of the two air-gap is 52 mm. With different axial lengths of the non-working air-gap, the flux density in the two air-gaps is computed and shown in Fig. 8.

Fig. 8 shows that the flux density in the working air-gap increases with the increase in the axial length of the non-working air-gap. However, the axial length of the armature winding decreases while the axial length of the non-working air-gap increases. The flux linkage of the ar-

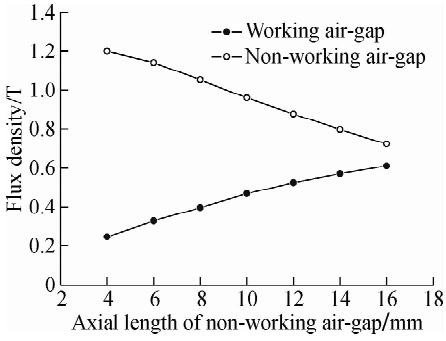

Fig. 8 Flux density in the two air-gaps

mature winding is relative to both the flux density in the working air-gap and the axial length of the armature winding. Therefore, the flux linkage of the armature winding does not increase with the increase in the axial length of the non-working air-gap. The computed results of the flux linkage are shown in Fig. 9. From Fig. 9, it can be seen that the optimal L_{gap2} is 12 mm, which is slightly higher than that of the analytical calculation (45/4 = 11.25 mm).

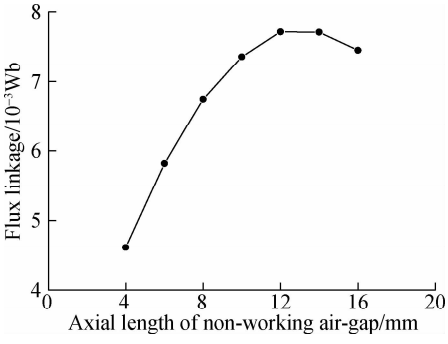

Fig. 9 Flux linkage of the armature winding

The numerical calculation results verify the correctness of the theoretical analysis. The figure 4 in the denominator of Eqs. (10) and (11) presents the pole-pairs p of the HIM. Therefore, the general formula to determine the axial length of the non-woking air-gap and ensure low magnetic saturation can be expressed as

$$L_{gap2} = \frac{D}{p} \tag{12}$$

Given that both the outer diameter and the total axial length of the HIM are constant, the volume of the HIM does not change. The power density of the HIM is defined as the output electrical power divided by the volume. With the variety in the axial lengths of the non-working air-gap, the numerical computing results of the power density are described in Fig. 10. In Fig. 10, the maximum value of the power density is selected as the reference of the per-unit value. The maximum value of the power density is reached when the axial length of the non-working air-gap is 14 mm, which deviates slightly from the calculation results. The reason is that the resistance of the armature winding decreases with the increase in the axial length of the non-working air-gap when the total axial length remains unchanged.

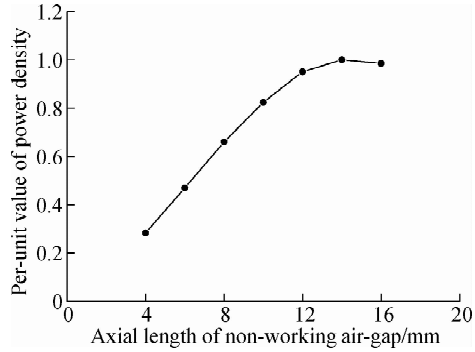

Fig. 10 Power density of the HIM

The optimal axial length of the non-working air-gap is 12 mm when considering the weight and manufacture of the HIM.

4 Experiment

A prototype HIM with 8-poles and 9-slots is designed and tested to verify the result of the theoretical analysis and numerical calculation. The specifications are listed in Tab. 1. The product photos are shown in Fig. 11.

Tab. 1 Primary specifications of the prototype HIM

Parameter	Value
Rated power/W	240
Rated rectified voltage /V	45
Stator inner diameter/mm	45
Stator outer diameter/(mm	75
Number of stator slots	9
Number of rotor poles	8
Rated DC current/A	5.33
Rated speed/(r · m^{-1})	3 000
Rated field voltage/V	31
Rated MMF/A	1 000
Number of turns of field coil	2 395
Air-gap length/mm	0.4

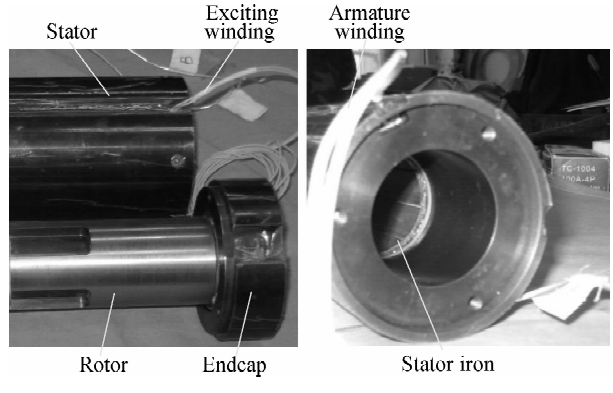

Fig. 11 Manufactured HIM

Fig. 12 presents the experimental result of the line-to-line back-EMF of the HIM under the no-load and rated speed. The experimental waveform has 9 small ripples within one electrical cycle owing to the influence of the stator slot-open. The amplitude of the measured back-EMF under no-load is 46 V. Compared with the finite element computation, there is little error, which is mainly caused by manufacturing tolerances and some variations in the magnetic properties.

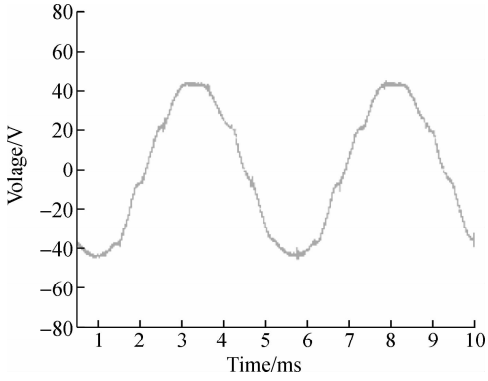

Fig. 12 Waveform of measured line-to-line back-EMF of the HIM under no-load

Some experiments are designed and implemented to validate the axial length allocation of the HIM. First, the line-to-line back-EMF of the HIM is recorded when the axial length of the armature winding L_{ea} is equal to 50 mm. The HIM prototype is disassembled, and the salient poles of the rotor are cut short until the axial length L_{ea} is equal to 45 mm. Then, the output voltage of the HIM prototype is measured again. After that, the measurement experiments are repeated when the axial length L_{ea} is equal to 42.5 and 40 mm. Fig. 13 describes the variations of the magnitude of the line-to-line back-EMF under different conditions. It can be seen that the amplitudes of the line-to-line back-EMF are almost equal under different situations when the excitation current is over 0.4 A. Therefore, considering material utilization, the optimal axial length of the armature winding is equal to 40 mm, which is consistent with the theoretical analysis and calculation.

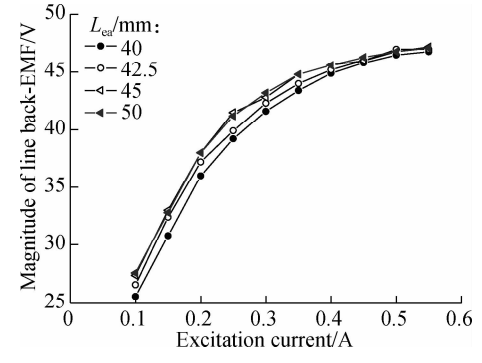

Fig. 13 Magnitude of the line-to-line back-EMF with different axial lengths L_{ea}

5 Conclusions

1) The design approach of the excitation winding proposed in this paper is practical and instrumental in determining the optimal parameters of the field winding.

2) The proper coefficient γ_L is in the range of 0.45 to 0.5, which applies both to the constant exciting magnetomotive force and to the constant exciting power.

3) The axial length of the non-working air-gap in the HIM should be equal to the ratio of the stator inner diameter and pole-pairs to ensure higher material utilization and lower magnetic saturation.

References

[1] Wang Q, Liu C J, Zou J B, et al. Numerical analysis and design optimization of a homopolar inductor machine used for flywheel energy storage[J]. *IEEE Transactions on Plasma Science*, 2013, **41**(5): 1290 − 1294. DOI: 10.1109/tps.2013.2243847.

[2] Tian X, Xu Y L, Wei S H. Design of a high-speed homopolar inductor machine for flywheel energy storage system[C]//2019 22*nd International Conference on Electrical Machines and Systems*. Harbin, China, 2019: 1 − 5. DOI: 10.1109/icems.2019.8921705.

[3] Ye C Y, Yang J T, Xu W, et al. A novel multi-unit outrotor homopolar inductor machine for flywheel energy storage system[J]. *IEEE Transactions on Magnetics*, 2018, **54**(11): 1 − 5. DOI: 10.1109/tmag.2018.2834956.

[4] Ye C Y, Yang J T, Liang X, et al. Investigation of a high-frequency pulsed alternator integrating motor and alternator[J]. *IEEE Transactions on Industrial Electronics*, 2019, **66**(4): 2592 − 2602. DOI: 10.1109/tie.2018.2842790.

[5] Yu K X, Yao J K, Xie X F, et al. Analysis of a novel excitation compensated homopolar inductor alternator used for capacitor charge power supply[J]. *IEEE Transactions on Plasma Science*, 2019, **47**(11): 5165 − 5171. DOI: 10.1109/tps.2019.2948029.

[6] Yang J T, Ye C Y, Liang X, et al. Study of a novel high-speed compensated pulsed alternator with multistage stator cores[J]. *IEEE Transactions on Plasma Science*, 2019, **47**(5): 2376 − 2381. DOI: 10.1109/tps.2018.2889564.

[7] Lou Z X, Yu K X, Wang L H, et al. Two-reaction theory of homopolar inductor alternator[J]. *IEEE Transactions on Energy Conversion*, 2010, **25**(3): 677 − 679. DOI: 10.1109/tec.2009.2038370.

[8] Ye C Y, Yang J T, Xiong F, et al. Relationship between homopolar inductor machine and wound-field synchronous machine[J]. *IEEE Transactions on Industrial Electronics*, 2020, **67**(2): 919 − 930. DOI: 10.1109/tie.2019.2898577.

[9] Bekhaled C, Hlioui S, Vido L, et al. 3D magnetic equivalent circuit model for homopolar hybrid excitation synchronous machines[C]//2007 *International Aegean Conference on Electrical Machines and Power Electronics*. Bodrum, Turkey, 2007: 575 − 580. DOI: 10.1109/

acemp. 2007. 4510568.
[10] Vido L, Gabsi M, Lecrivain M, et al. Homopolar and bipolar hybrid excitation synchronous machines[C]//*IEEE International Conference on Electric Machines and Drives*. San Antonio, TX, USA, 2005: 1212 - 1218. DOI: 10. 1109/iemdc. 2005. 195876.
[11] Fu X H, Zou J B. Numerical analysis on the magnetic field of hybrid exciting synchronous generator[J]. *IEEE Transactions on Magnetics*, 2009, **45**(10): 4590 - 4593. DOI: 10. 1109/tmag. 2009. 2023625.
[12] Yang J T, Ye C Y, Huang S D, et al. Analysis of the electromagnetic performance of homopolar inductor machine through nonlinear magnetic equivalent circuit and air-gap permeance function[J]. *IEEE Transactions on Industry Applications*, 2020, **56**(1): 267 - 276. DOI: 10. 1109/tia. 2019. 2954803.
[13] Yang J T, Ye C Y, Liang X, et al. Investigation of a two-dimensional analytical model of the homopolar inductor alternator[J]. *IEEE Transactions on Applied Superconductivity*, 2018, **28**(3): 5205205-1 - 5205205-5. DOI: 10. 1109/tasc. 2018. 2802480.
[14] Lou Z X, Yu K X, Ren Z G, et al. Analysis of homopolar inductor alternator for high reliability high power density applications[C]//2009 *IEEE 6th International Power Electronics and Motion Control Conference*. Wuhan, China, 2009: 841 - 844. DOI: 10. 1109/ipemc. 2009. 5157501.
[15] Fu X H, Lin M Y, Yu H T, et al. A novel 2-D simplified model for investigating the rotor shape of homopolar inductor alternator[C]//2012 *Sixth International Conference on Electromagnetic Field Problems and Applications*. Dalian, China, 2012: 1 - 4. DOI: 10. 1109/icef. 2012. 6310387.
[16] Orlova S, Pugachov V, Levin N, et al. Non-overlapping concentrated windings in homopolar inductor machines[C]//*Proceedings of International Symposium on Power Electronics, Electrical Drives, Automation and Motion*. Pisa, Italy, 2010: 282 - 286. DOI: 10. 1109/SPEEDAM. 2010. 5544764.
[17] Fu X H, Lin M Y, Yu H T, et al. Calculation and analysis of iron loss in homopolar inductor alternator[J]. *IEEE Transactions on Magnetics*, 2012, **48**(11): 3466 - 3469. DOI: 10. 1109/tmag. 2012. 2202098.
[18] Xin Q M, Yu K X, Ren Z A, et al. Inductance mathematic model of a homopolar inductor alternator in a novel pulse capacitor charge power supply[J]. *IEEE Transactions on Plasma Science*, 2013, **41**(5): 1231 - 1236. DOI: 10. 1109/tps. 2013. 2251751.
[19] Ye C Y, Yang J T, Liang X, et al. Design and research of a high-speed and high-frequency pulsed alternator[J]. *IEEE Transactions on Plasma Science*, 2017, **45**(7): 1512 - 1518. DOI: 10. 1109/tps. 2017. 2705984.
[20] Ren Z A, Yu K X, Xin Q M, et al. Performance of homopolar inductor alternator with diode-bridge rectifier and capacitive load[J]. *IEEE Transactions on Industrial Electronics*, 2013, **60**(11): 4891 - 4902. DOI: 10. 1109/tie. 2012. 2227908.
[21] Narayanan P M V, Anu G, Mini V P. Design development and performance analysis of homopolar inductor pulsed alternator[C]//2018 *International CET Conference on Control, Communication, and Computing*. Trivandrum, India, 2018: 39 - 44. DOI: 10. 1109/cetic4. 2018. 8530946.

单极性感应子电机励磁系统分析与设计

付兴贺　付相达　徐彧田　何　航

（东南大学电气工程学院，南京 210096）

摘要：为了建立单极性感应子电机励磁系统的设计方法和评价准则，对单极性感应子电机的励磁系统开展分析与设计. 利用有限元方法计算电机内的三维电磁场，揭示磁场分布规律和特性；利用解析方法讨论励磁绕组的设计流程；利用数值计算方法研究电枢绕组与励磁绕组的轴向长度比例关系及工作气隙与非工作气隙的轴向长度比例关系. 设计并制造实验样机，实验研究验证了理论分析与数值计算结果的正确性. 结果表明：所建立的励磁绕组设计方法有效、可行；在恒定励磁磁动势或恒定励磁功率条件下，电枢绕组与励磁绕组的轴向长度比例系数的合理取值范围为 0.45 ~ 0.5；非工作气隙最佳轴向长度可由定子内径与极对数之比确定.

关键词：单极性感应子电机；励磁系统；励磁绕组；轴向长度比

中图分类号：TM354